MULTI-CRITERIA CALIBRATION OF A WELDING HEAT-TRANSFER MODEL: BALANCING GEOMETRIC AND TEMPERATURE-BASED OBJECTIVES

Mišo B. BJELIĆ[1], Branko S. RADIČEVIĆ[1], Aleksandra V. PETROVIĆ[*1], Mladen S. RASINAC[1], Miroslav M. MIJAJLOVIĆ[2]

[1] University of Kragujevac, Faculty of Mechanical and Civil Engineering in Kraljevo, Serbia

[2] University of Niš, Faculty of Mechanical Engineering, Niš, Serbia

[*] Corresponding author; E-mail: petrovic.a@mfkv.kg.ac.rs

Calibration of heat-source parameters and boundary heat losses is essential for reliable numerical welding simulations. This paper applies Grey relational analysis with entropy-based weighting to calibrate a three-dimensional heat-transfer model for gas metal arc welding of P355GH steel. Eight parameters are calibrated simultaneously: five describing the Goldak double-ellipsoidal heat source and three describing convective and radiative losses. Latin hypercube sampling with 80 combinations is used to explore the parameter space, and five objective functions are defined: three geometry-based and two temperature-based. Three calibration scenarios are compared: geometry-based, temperature-based, and combined, revealing a pronounced trade-off between geometric and thermal criteria. The combined scenario yields physically plausible parameter values and balanced prediction quality for both fusion-zone geometry and peak temperature indicators, and is therefore recommended for practical calibration of welding heat-transfer models.

Keywords*: double-ellipsoidal heat source, Grey relational analysis, Latin hypercube sampling, entropy weights, GMAW, calibration*

1. Introduction

Numerical simulations of welding processes are widely used to analyse temperature fields, distortions, and residual stresses, as well as to predict microstructure and hardness in the heat-affected zone [1,2]. Their increasing industrial use is reflected in documents such as ISO 18166 [1], which specifies recommended workflows for numerical welding simulations. The predictive capability of such simulations strongly depends on the adopted heat-transfer and heat-input models and on the reliability of calibrated model parameters.

For arc welding processes, the Goldak double-ellipsoidal heat-source model [3] has become a standard choice because it combines a plausible physical basis with numerical efficiency. In practice, however, the corresponding parameters - geometric semi-axes and arc efficiency are not fixed material constants, are often tuned by trial-and-error [4] and depend on process conditions [5,6]. Similar difficulties arise for boundary conditions, particularly emissivity [7] and convective heat-transfer coefficients [8], whose effects on the temperature field can partly compensate changes in heat input [9]. As a result, different combinations of heat-source and boundary parameters may produce similar weld geometries but markedly different thermal responses, leading to non-uniqueness in model calibration [9].

Previous studies have addressed calibration of Goldak-type models using analytical approaches [10], inverse methods [11], metaheuristic optimization and machine-learning approaches [12], but most of them focused primarily on weld-bead geometry (width and penetration). Since microstructure evolution and hardness are governed by thermal cycles, such geometry-only calibration does not guarantee physically realistic temperature predictions [9]. Previous work examined temperature-based calibration using simulated annealing [13] and multi-objective, geometry-based calibration [14]. However, the combined influence of heat-input and surface heat-loss parameters, and the role of different objective-function sets, have not been systematically quantified.

The aim of this study is to develop and evaluate a multi-criteria calibration framework for a welding heat-transfer model that simultaneously considers weld geometry and temperature-based indicators. A three-dimensional quasi-stationary model with a Goldak double-ellipsoidal heat source is calibrated for GMAW of P355GH steel, using Latin hypercube sampling [15] to generate 80 combinations of eight input parameters. Five objective functions are defined from weld cross-section geometry and thermocouple peak temperatures; Grey relational analysis [16] with entropy-based weighting is then used to rank the alternatives under three scenarios: geometry-only, temperature-only, and combined. The study quantifies the trade-off between geometric and thermal objectives, identifies physically consistent parameter ranges, and formulates recommendations for practical calibration of welding simulations.

2. Materials and methods

2.1. Experimental data

Calibration of the welding heat-transfer model was performed using experimental data obtained from gas metal arc welding of P355GH steel. Welding was conducted on a 300×150×5 [mm] plate in a bead-on-plate configuration at an initial temperature of T_0=20 [°C] with the following parameters: arc voltage U=21.3 [V], welding current I=207 [A], welding speed v=8 [mm/s] and electrode wire diameter d_w=1.2 [mm]. A shielding gas mixture of 82% Ar and 18% CO_2 was supplied at a flow rate of 12 [l/min].

The experimental dataset comprises two groups of quantities. The first group describes the weld cross-section geometry obtained by macro-sectioning and digitization, Fig. 1a: weld face width W_{exp}, penetration depth D_{exp}, and fusion-zone cross-sectional area A_{exp}.

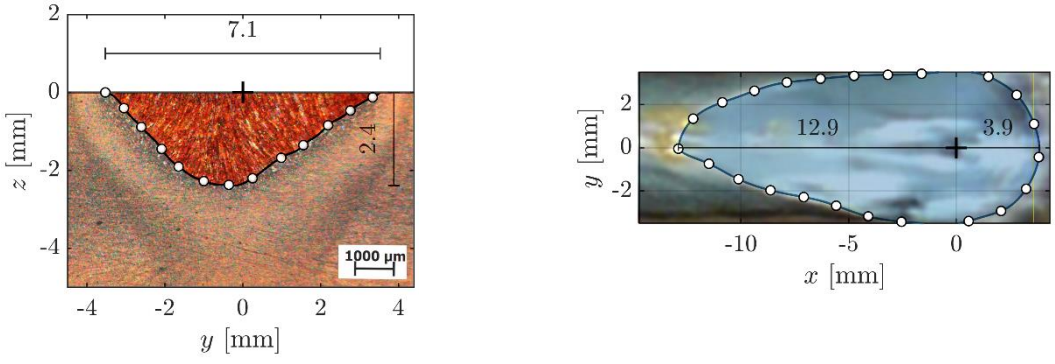

Figure 1. Digitized weld geometry: (a) Weld cross-section with extracted W_{exp}, D_{exp} and A_{exp}, (b) digitized end-crater contour in the with extracted a_f^{exp} and a_r^{exp}

The corresponding measured values are summarized in Tab. 1. In addition to the geometric targets, Tab. 1 also reports the crater-based semi-axes a_f^{exp} and a_r^{exp} extracted from Fig. 1b. Since the end-

crater forms during arc extinction under transient cooling conditions, its geometry does not necessarily correspond to the quasi-stationary melt pool; consequently, a_f^{exp} and a_r^{exp} are treated as approximate reference values. The peak surface temperatures $T_{exp,1}^{max}$ and $T_{exp,2}^{max}$ were measured by thermocouples at $x_{1,2}$=230 [mm], y_1=10 [mm] and y_2=20 [mm], respectively, Fig. 2.

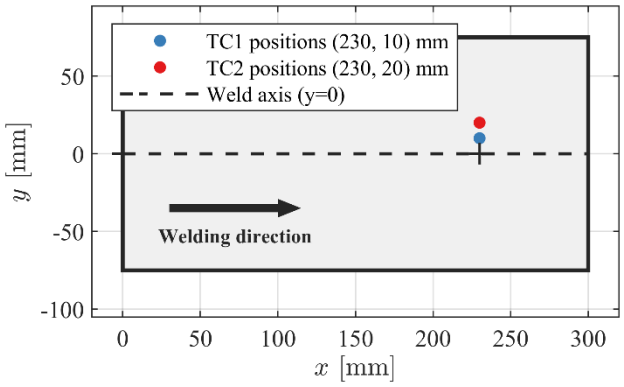

Figure 2. Thermocouple locations

Table 1. Experimental calibration targets

Parameter	Value
W_{exp}	7.1 [mm]
D_{exp}	2.4 [mm]
A_{exp}	9.6 [mm^2]
a_f^{exp}	3.9 [mm]
a_r^{exp}	12.9 [mm]
$T_{exp,1}^{max}$	373 [°C]
$T_{exp,2}^{max}$	231 [°C]

Temperature-dependent thermophysical properties ($\rho(T)$, $\lambda(T)$, and $c_p(T)$) of P355GH steel were determined using the methodology described in [13]. The filler material was not modeled explicitly. Since the Goldak model represents heat input rather than mass addition, the computational domain was treated as homogeneous (base material), while the influence of filler deposition is captured indirectly through the calibrated equivalent heat-input parameters. This simplification neglects the weld reinforcement geometry and the associated change in surface boundary conditions above the weld pool. In the present bead-on-plate configuration with moderate reinforcement, the effect is expected to be secondary, but it may contribute to systematic differences between calibrated and physically expected values of the geometric semi-axes, particularly b_h and c_h.

2.2. Goldak double-ellipsoidal heat-source model

The Goldak double-ellipsoidal model was used to represent the spatial distribution of heat input. The front and rear semi-ellipsoids allow different heat distributions ahead of and behind the arc, which better reproduces real melt pool asymmetry. The coordinate system was defined with the x-axis aligned with the travel direction, the y-axis transverse to travel, and the z-axis through the plate thickness. The volumetric power density in the front (q_f) and rear (q_r) semi-ellipsoids is given by Eqs. (1)-(2):

$$q_f(x,y,z) = \frac{6\sqrt{3}\, f_f\, Q}{\pi\sqrt{\pi}\, a_f\, b_h\, c_h} \exp\left(-3\frac{x^2}{a_f^2} - 3\frac{y^2}{b_h^2} - 3\frac{z^2}{c_h^2}\right) \quad (1)$$

$$q_r(x,y,z) = \frac{6\sqrt{3}\, f_r\, Q}{\pi\sqrt{\pi}\, a_r\, b_h\, c_h} \exp\left(-3\frac{x^2}{a_r^2} - 3\frac{y^2}{b_h^2} - 3\frac{z^2}{c_h^2}\right) \quad (2)$$

where a_f and a_r are the semi-axes in the welding direction for the front and rear ellipsoids, b_h is the transverse semi-axis, and c_h is the through-thickness semi-axis. The power fractions satisfy relation f_f+f_r=2 with f_f=2a_f/(a_f+a_r) and f_r=2a_r/(a_f+a_r). The effective heat-source power is defined as Q=ηUI, where η is the arc efficiency, U is arc voltage and I is current.

To improve numerical robustness and enable consistent comparison across parameter combinations, the geometric parameters were expressed using dimensionless ratios relative to reference values estimated from the experimental weld geometry: $b_h=W_{exp}/2$, $c_h=D_{exp}$, $a_f=a_f^{exp}$, $a_r=a_r^{exp}$. This parameterization defines the search space in a scale-consistent form and facilitates exploration with a limited number of simulations.

2.3. Numerical simulation

A three-dimensional quasi-steady heat-transfer model formulated in a moving coordinate system attached to the heat source was employed. Using the transformation $\xi=x-vt$, the transient heat conduction problem is written in quasi-steady form and solved iteratively until convergence. The governing equation is given by Eq. (3), where $\rho=\rho(T)$, $c_p=c_p(T)$, and $\lambda=\lambda(T)$ denote density, specific heat, and thermal conductivity, L is the latent heat and q_l is the volumetric power density defined by the Goldak model ($q_l=q_f$ for $\xi\geq 0$, $q_l=q_r$ for $\xi<0$).

$$-\rho v_w\left(c_p+L\frac{\partial f_{liq}}{\partial T}\right)\frac{\partial T}{\partial \xi}=\lambda\left(\frac{\partial^2 T}{\partial \xi^2}+\frac{\partial^2 T}{\partial y^2}+\frac{\partial^2 T}{\partial z^2}\right)+q_l \tag{3}$$

The governing equation was solved numerically using a finite difference scheme combined with a multigrid strategy and successive over-relaxation, following the computational procedure described and verified in [14]. The minimum grid spacing was 0.25 mm. Convective and radiative heat losses were applied on the top and bottom surfaces, Eq. (4):

$$-\lambda\frac{\partial T}{\partial n}=h_{t/b}\left(T-T_\infty\right)+\varepsilon\sigma\left(T^4-T_\infty^4\right) \tag{4}$$

using convection coefficients for top and bottom surface, h_t and h_b, emissivity ε, ambient temperature T_∞, and the Stefan-Boltzmann constant σ. The lateral surfaces were treated as adiabatic.

2.4. Parameter space and objective functions

A parameter space of eight variables was defined. The heat input was described by four dimensionless geometric ratios of the Goldak model (a_f/a_f^{exp}, a_r/a_r^{exp}, b_h/b_h^{exp}, and c_h/c_h^{exp}) and the arc efficiency η. Heat losses were described by surface emissivity ε and convection coefficients for the top and bottom surfaces (h_t and h_b). The parameter ranges are summarized in Tab. 2.

Table 2. Parameter ranges

Parameter	Min	Max	Parameter	Min	Max
η	0.4	0.9	a_f/a_f^{exp}	0.50	1.50
ε	0.3	0.9	a_r/a_r^{exp}	0.50	1.50
h_t	5	50	b_h/b_h^{exp}	0.50	1.50
h_b	5	30	c_h/c_h^{exp}	0.50	1.50

The range of η was intentionally set wider than commonly reported GMAW values [5,6] (typically (0.65÷0.85) to allow the sampling to explore compensatory effects between arc efficiency and boundary conditions without constraining the search a priori.

The parameter space was sampled using Latin hypercube sampling (LHS) with 80 combinations, providing 10 samples per parameter, which ensures reasonable space-filling coverage for the eight-dimensional domain, as illustrated by representative projections in Fig. 3.

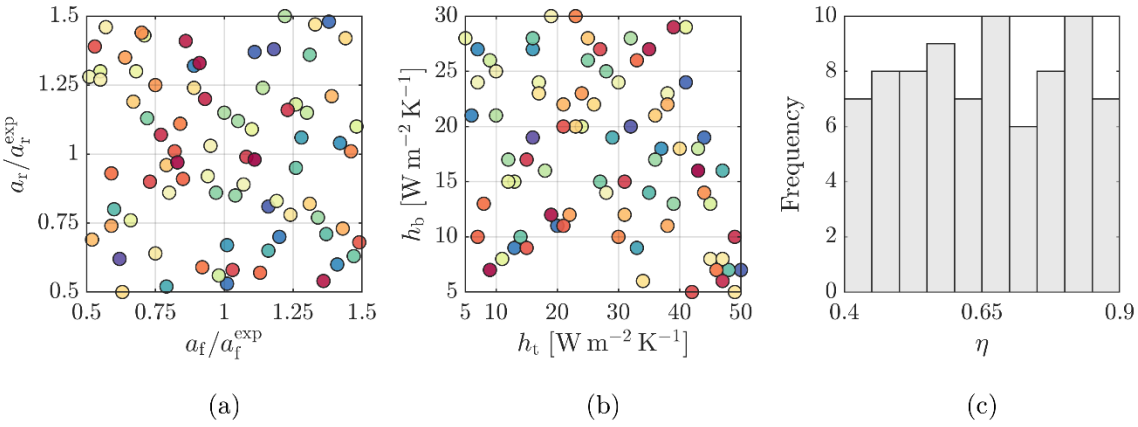

Figure 3. Representative LHS projections of heat-source and boundary-condition parameters: (a) a_f/a_f^{exp} vs. a_r/a_r^{exp}; (b) h_t vs. h_b; (c) marginal distribution of η.

Objective functions were defined as normalized squared deviations between simulated and experimental quantities. Geometry-based criteria were computed from W, D, and A, Eq. (5). Fusion-zone geometry was evaluated using the liquidus isotherm (T_{liq} = 1509 [°C]).

$$F_W = \left(\frac{W_{sim} - W_{exp}}{W_{exp}} \right)^2, \quad F_D = \left(\frac{D_{sim} - D_{exp}}{D_{exp}} \right)^2, \quad F_A = \left(\frac{A_{sim} - A_{exp}}{A_{exp}} \right)^2 \tag{5}$$

Temperature-based criteria were defined using the maximum temperatures measured at y_1=10 mm and y_2=20 mm from the weld centerline, Eq. (6).

$$F_{T1} = \left(\frac{T_{sim,1}^{max} - T_{exp,1}^{max}}{T_{exp,1}^{max}} \right)^2, \qquad F_{T2} = \left(\frac{T_{sim,2}^{max} - T_{exp,2}^{max}}{T_{exp,2}^{max}} \right)^2 \tag{6}$$

All criteria follow the "smaller-is-better" convention. Multi-criteria ranking was performed using Grey relational analysis (GRA). For each scenario, criteria were first normalized using the "smaller-is-better" transformation, and the grey relational coefficient was computed with the resolution coefficient ζ=0.5. To compute the grey relational coefficient (GRC), the objective functions were first normalized to comparable, dimensionless sequences. For each alternative i and objective k, the absolute deviation from the reference sequence is defined as $\Delta_i(k)=|x_0(k)-x_i(k)|$, where $x_0(k)$ denotes the ideal (best) normalized value and $x_i(k)$ is the corresponding normalized value of alternative i. Let $\Delta_{min}=\min_{i,k}\Delta_i(k)$ and $\Delta_{max}=\max_{i,k}\Delta_i(k)$. The grey relational coefficient is then evaluated as $\xi_i(k)=(\Delta_{min}+\zeta\Delta_{max})/(\Delta_i(k)+\zeta\Delta_{max})$, and the overall grey relational grade (GRG) of alternative i is obtained by aggregation across all objectives as $GRG_i=\sum_k w_k \xi_i(k)$, where w_k are the entropy-based weights, $\sum_k w_k$ =1. A small constant was used to avoid ln(0) in entropy calculations.

Three optimization scenarios were considered: (A) geometry-based criteria (F_W, F_D, F_A), (B) temperature-based criteria (F_{T1}, F_{T2}), and (C) the combined set (F_W, F_D, F_A, F_{T1}, F_{T2}).

3. Results and discussion

3.1. Entropy-based weights and criterion conflict

Entropy-based weights quantify the discriminating power of each objective function across the 80 LHS samples, Tab. 3. In Scenario A (geometry only), the cross-sectional area function F_A receives the highest weight (0.421), which is expected because the area integrates the effects of both width and depth variations and therefore possesses greater discriminatory power. Width (F_W: 0.358) and depth (F_D: 0.221) carry lower influence. Scenario B (temperature only) shows balanced weights between near-weld (F_{T1}: 0.556) and far-weld (F_{T2}: 0.444) indicators, with the near-weld position exhibiting slightly greater sensitivity to parameter changes. In the combined Scenario C, weights are more uniform, with geometric criteria accounting for 56.6% and temperature criteria for 43.4% of total influence. This distribution is favorable because it prevents the temperature indicators from entirely suppressing the geometric fidelity of the fusion zone.

Table 3. Entropy weights of the objective functions for each scenario

Scenario	F_W	F_D	F_A	F_{T1}	F_{T2}
A	0.358	0.221	0.421	–	–
B	–	–	–	0.556	0.444
C	0.203	0.125	0.239	0.241	0.193

Pearson's correlation matrix, Tab. 4, reveals strong positive correlations within each criterion group and significant negative correlations between them. Geometric functions are mutually correlated (F_W-F_D: r=0.77; F_W-F_A: r=0.73; F_D-F_A: r=0.87), indicating that improvement in one geometric measure generally accompanies improvement in the others. Temperature functions are nearly perfectly correlated (F_{T1}-F_{T2}: r=0.99), meaning that both thermocouple positions respond almost identically to parameter variations under the examined conditions. This near-redundancy suggests that future studies could benefit from more diverse thermal indicators, such as cooling rates or $t_{8/5}$ times. Negative correlations between geometric and temperature groups range from moderate to strong (F_D-F_{T1}: r=–0.31; F_W-F_{T1}: r =–0.56), confirming that parameter sets optimizing fusion-zone geometry systematically underpredict near-weld temperatures. This conflict weakens with distance from the weld (F_W-F_{T2}: r=–0.49), suggesting that the discrepancy is most acute in the immediate vicinity of the fusion zone, where the competing influences of heat-source distribution and heat dissipation overlap most strongly.

Table 4. Pearson correlation matrix of the objective functions

	F_W	F_D	F_A	F_{T1}	F_{T2}
F_W	1.00	0.77	0.73	–0.56	–0.49
F_D		1.00	0.87	–0.32	–0.26
F_A			1.00	–0.14	–0.07
F_{T1}				1.00	0.99
F_{T2}					1.00

This trade-off reflects competing calibration directions within the adopted model: increasing arc efficiency η enlarges both the fusion zone and the surrounding temperature field, while geometric semi-axes can partly compensate weld dimensions without proportionally reducing temperatures [9]. Figure 4 visualizes this conflict across LHS samples, with Scenario A favoring geometry, Scenario B favoring temperature, and Scenario C achieving a balanced compromise.

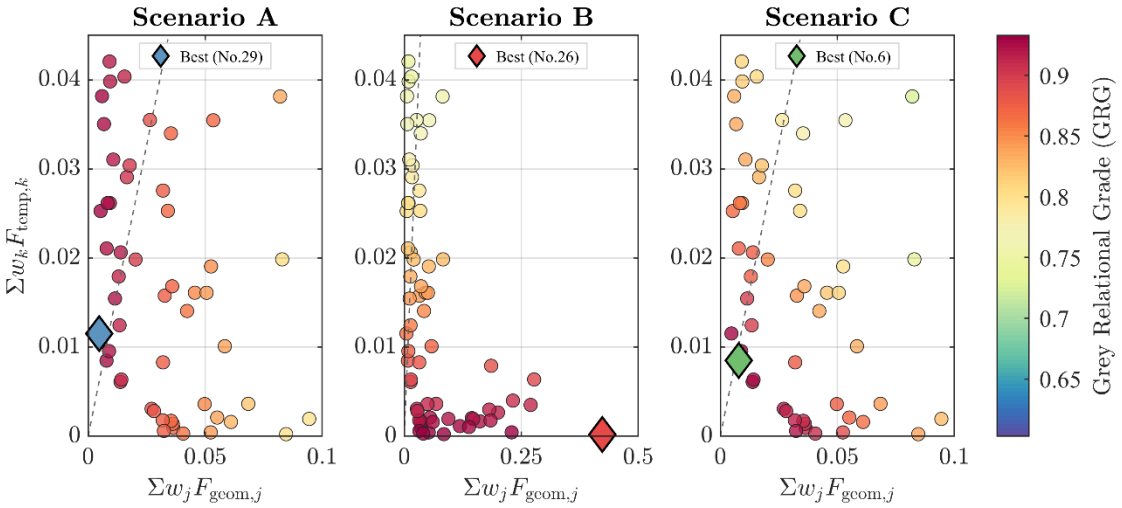

Figure 4. Trade-off between ΣF_{geom} and ΣF_{temp} for scenarios A–C

3.2. Scenario-specific optima (A–C)

A comparative overview of the optimal parameters for each scenario is given in Tab. 5, together with the corresponding grey relational grade. Arc efficiency η shows the largest inter-scenario variation: Scenario A yields η=0.66, Scenario B yields η=0.46, and Scenario C yields η=0.61. Comparison with literature data for GMAW with Ar/CO_2 shielding [5-6, 17-18] indicates that the Scenario C value lies near the lower bound of commonly reported values, whereas Scenario B yields a markedly lower η. This is consistent with the near-perfect correlation between the two temperature criteria (FT1-FT2: r=0.99, Tab. 4), which effectively reduces Scenario B to a single-criterion optimization with insufficient constraints to prevent parameter drift. This indicates that temperature-only calibration can push η toward compensatory values within the adopted model and objective set, rather than toward a uniquely physical arc-efficiency estimate.

Table 5. Optimal model parameters for each scenario

Parameter	Scenario A (no. 29)	Scenario B (no. 26)	Scenario C (no. 6)
η	0.66	0.46	0.61
ε	0.60	0.68	0.79
h_t	9	10	20
h_b	26	21	11
a_f/a_f^{exp}	0.98	1.22	1.01
a_r/a_r^{exp}	0.56	1.50	0.53
b_h/b_h^{exp}	1.34	1.41	0.86
c_h/c_h^{exp}	1.12	1.14	0.68
GRG	0.980	0.997	0.933

In Scenario C, the ratio a_f/a_f^{exp}=1.01 indicates excellent agreement of the front semi-axis with the reference value, which is important for predicting thermal cycles ahead of the source. The ratio b_h/b_h^{exp}=0.86 is reasonably consistent with Goldak's original recommendation of adopting geometric parameters approximately 10% below their experimental values, although the deviation may also reflect

limitations of the ellipsoidal geometry in reproducing the actual fusion-zone shape, which can be asymmetric and influenced by melt-pool convection patterns. In contrast, c_h/c_h^{exp}=0.68 deviates considerably from this guideline, consistent with the modelling simplification discussed in Section 2.1: the model concentrates heat input closer to the surface to compensate for unmodelled reinforcement geometry and weld-pool convection, effects that are more pronounced in the depth direction. Scenario B exhibits extreme values (a_r/a_r^{exp}=1.50), further illustrating the limitations of single-criterion calibration.

The optimal convective coefficients for Scenario C (h_t=20 [Wm^{-2}K^{-1}], h_b=11 [Wm^{-2}K^{-1}]) are of the expected order of magnitude for natural convection [8]. The higher value on the upper surface is consistent with buoyancy-driven convection above the heated plate. The emissivity ε=0.79 is likewise plausible for oxidized steel surfaces at elevated temperatures [7].

3.3. Solution quality and practical implications

Figure 5 provides a direct visual comparison of the three scenario-specific optima with the experimental data. The peak temperature profile, Fig. 5a, shows that Scenario B closely reproduces the measured thermocouple values, while Scenarios A and C overpredict the peak temperatures. The fusion-zone contour, Fig. 5b, confirms the opposite trend: Scenarios A and C closely reproduce the experimental cross-section, while Scenario B yields a markedly smaller fusion zone.

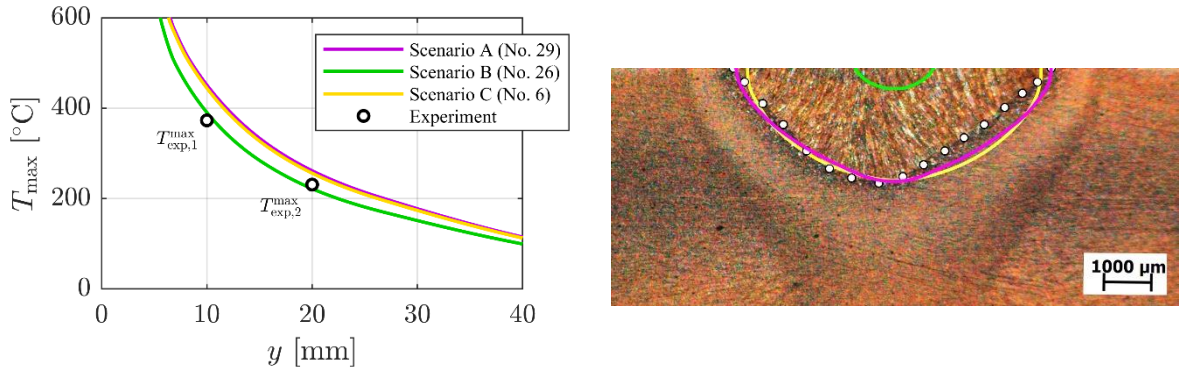

Figure 5. Comparison of the three scenario-specific optima with experimental data: (a) peak surface temperature profiles T_{max}(y); (b) fusion-zone contours (T = 1509 °C)

Group-level error sums and a balance coefficient B=min(ΣF_{geom}, ΣF_{temp})/max(ΣF_{geom}, ΣF_{temp}) quantify the trade-off between geometric and thermal objectives, Tab. 6. Scenario B achieves near-perfect temperature matching (ΣF_{temp}=0.001) but at the expense of a very large geometric error (ΣF_{geom}=2.193), resulting in an extremely poor balance. Scenario A shows low geometric error (0.021) but a higher temperature discrepancy (0.052), yielding a balance of 0.40. The combined Scenario C provides the best balance (0.95), with comparable group errors (ΣF_{geom}=0.036, ΣF_{temp}=0.038) and a total error comparable to Scenario A.

Table 6. Solution quality metrics for the optimal solutions

Sce. / opt. sol.	ΣF_{geom}	ΣF_{temp}	Total	Balance
A / (no. 29)	0.021	0.052	0.073	0.40
B / (no. 26)	2.193	0.001	2.194	≈0
C / (no. 6)	0.036	0.038	0.074	0.95

Normalized objective values, Tab. 7, confirm that Scenario C maintains high performance across all five criteria (≥0.92), whereas Scenario B collapses for the geometric objectives. For the Scenario C optimum, the simulated weld width and penetration depth are slightly below the experimental values, while the cross-sectional area and peak temperatures at both thermocouple positions are slightly over-predicted. These results support combined calibration as the preferred strategy when the model is intended to reproduce both fusion-zone geometry and temperature-based indicators, while single-criterion calibration may yield parameter sets that are accurate only within a narrow subset of targets.

Table 7. Normalized objective function values (1 = best, 0 = worst in sample set)

Objective	Scenario A	Scenario B	Scenario C
F_W	0.992	0.000	0.973
F_D	1.000	0.000	0.997
F_A	0.983	0.000	0.980
F_{T1}	0.902	1.000	0.925
F_{T2}	0.935	0.997	0.957

Table 8 lists the five best-ranked parameter sets under the combined Scenario C criteria together with the key calibration metrics.

Table 8. Top five ranked solutions for Scenario C

Rank	No.	GRG	η	b_h/b_h^{exp}	c_h/c_h^{exp}	a_r/a_r^{exp}	ΣF_{geom}	ΣF_{temp}	Balance
1.	6	0.933	0.61	0.86	0.68	0.53	0.036	0.038	0.95
2.	7	0.928	0.57	0.98	0.7	0.7	0.083	0.028	0.34
3.	29	0.927	0.66	1.34	1.12	0.56	0.021	0.052	0.40
4.	63	0.926	0.67	0.69	0.83	0.59	0.070	0.028	0.40
5.	57	0.924	0.67	1.20	1.22	0.74	0.042	0.043	0.98

The GRG values form a narrow band (0.924÷0.933), indicating that the optimum belongs to a near-optimal cluster rather than an isolated point. Decomposition of the GRG, for the optimal solution (No. 6) confirms well-balanced performance: all individual grey relational coefficients exceed 0.86, with the largest contributions from F_A ($\xi \cdot w = 0.229$) and F_{T1} ($\xi \cdot w = 0.209$), reflecting both high GRC values and substantial entropy weights.

3.4. Near-optimal region and non-uniqueness

Sixteen samples (20% of the total) achieve GRG values within 5% of the Scenario C optimum. Within this near-optimal region, arc efficiency spans a comparatively narrow interval (η=0.45÷0.73), confirming its primary role in controlling the net energy input. In contrast, all four geometric ratios (a_f/a_f^{exp}, a_r/a_r^{exp}, b_h/b_h^{exp}, c_h/c_h^{exp}) vary across nearly the entire search domain (approximately 0.50÷1.50), as confirmed by the top-ranked solutions in Tab. 8 (b_h/b_h^{exp}=0.69÷1.34 and c_h/c_h^{exp}=0.68÷1.22), indicating that different ellipsoidal shapes can satisfy the same calibration targets. Emissivity also exhibits a wide range (ε=0.35÷0.90), which is physically expected since conduction and surface convection dominate the heat balance within the plate, while radiation becomes significant only at higher temperatures and larger exposed surface areas.

In practical terms, calibration should therefore aim not at identifying a single point in parameter space, but at delineating a stable region of solutions that yields satisfactory results for both criterion groups. Within such a region, the final parameter selection can be guided by additional criteria such as the physical plausibility of individual parameter values or the specific requirements of the intended application.

4. Conclusion

This study evaluated three calibration scenarios (geometry-based, temperature-based, and combined) for a three-dimensional welding heat-transfer model applied to GMAW of P355GH steel, using Grey relational analysis with entropy-based weighting to rank 80 Latin hypercube samples across five objective functions.

The results reveal a clear trade-off between geometric and thermal criteria, reflected by negative correlations between their objective functions, while the two peak-temperature indicators exhibit high redundancy. Geometry-only calibration provides excellent agreement in weld width, penetration, and area, but yields substantially larger discrepancies in the peak temperature indicators. Temperature-only calibration matches peak temperatures very closely, yet produces poor weld geometry and, within the adopted modelling assumptions, an implausibly low arc-efficiency estimate (η=0.46) for the investigated GMAW conditions.

The combined scenario offers the most balanced solution, with comparable error levels across geometric and peak temperature objectives, GRA-based normalized performance above 0.92 for all criteria, and parameter values remaining within physically plausible ranges for arc efficiency, convective coefficients, and emissivity. In this context, arc efficiency should be interpreted as an effective net heat-input parameter within the modelling framework, rather than as a direct experimental measure. Analysis of near-optimal alternatives indicates moderate parameter variability of the calibration problem and confirms the presence of a near-optimal parameter region, rather than a single unique optimum, that provides similar calibration quality.

From a practical perspective, the study shows that reliable calibration of welding simulations benefits from simultaneous inclusion of both fusion-zone geometry and temperature-based indicators; single-criterion strategies are more prone to non-unique and physically questionable parameter sets. Future work will extend the methodology to other materials and welding conditions, incorporate more informative thermal descriptors (e.g., cooling times and spatially separated measurements), and validate the calibrated parameters against independent experiments with different plate thicknesses or welding regimes.

Acknowledgement

The authors acknowledge the support of the Ministry of Science, Technological Development and Innovation of the Republic of Serbia (Contract No. 451-03-34/2026-03/200108). The research is aligned with the United Nations 2030 Agenda for Sustainable Development, particularly SDG 9: “Build resilient infrastructure, promote inclusive and sustainable industrialization and foster innovation.”

Nomenclature

Latin symbols

A	–	weld cross-section area, [mm²]	Q	–	effective arc power ($Q=\eta UI$), [W]
a_f	–	front half-ellipsoid semi-axis in travel direction (x), [mm]	q_f	–	volumetric power density (front ellipsoid), [Wm⁻³]
a_r	–	rear half-ellipsoid semi-axis in travel direction (x), [mm]	q_l	–	volumetric heat source (power density), [Wm⁻³]
b_h	–	semi-axis in transverse direction (y), [mm]	q_r	–	volumetric power density (rear ellipsoid), [Wm⁻³]
c_h	–	semi-axis in thickness direction (z), [mm]	t	–	time, [s]
c_p	–	specific heat capacity, [Jkg⁻¹K⁻¹]	T	–	temperature, [°C]
D	–	penetration depth, [mm]	T_0	–	initial temperature, [°C]
F_A	–	objective function for area, [–]	T_∞	–	ambient temperature, [°C]
F_D	–	objective function for penetration depth, [–]	T_{liq}	–	liquidus temperature, [°C]
f_f	–	front power fraction coefficient, [–]	U	–	arc voltage, [V]
f_r	–	rear power fraction coefficient, [–]	v	–	welding speed, [mms⁻¹]
F_{T1}	–	objective function for peak temperature at y_1, [–]	W	–	weld bead width, [mm]
F_{T2}	–	objective function for peak temperature at y_2, [–]	w_k	–	weight of criterion k in GRG, [–]
F_W	–	objective function for weld width, [–]	x	–	spatial coordinate, [mm]
h_b	–	convection coefficient (bottom surface), [Wm⁻²K⁻¹]	y	–	spatial coordinate, [mm]
h_t	–	convection coefficient (top surface), [Wm⁻²K⁻¹]	y_1	–	thermocouple offset from weld centerline, [mm]
I	–	welding current, [A]	y_2	–	thermocouple offset from weld centerline, [mm]
L	–	latent heat of fusion, [Jkg⁻¹]	z	–	spatial coordinate, [mm]

Greek symbols

$\Delta_{i(k)}$	–	deviation in GRA for alternative i and criterion k, [–]	λ	–	thermal conductivity, [Wm⁻¹K⁻¹]
Δ_{max}	–	maximum deviation in GRA, [–]	ρ	–	density, [kgm⁻³]
Δ_{min}	–	minimum deviation in GRA, [–]	σ	–	Stefan–Boltzmann constant, [Wm⁻²K⁻⁴]
ε	–	emissivity, [–]	ξ	–	moving coordinate system ($\xi=x-vt$), [mm]
η	–	arc efficiency, [–]	ζ	–	GRA resolution coefficient, [–]

Subscripts

0	–	initial value, [–]	∞	–	ambient, [–]
1	–	thermocouple location index, [–]	k	–	criterion index, [–]
2	–	thermocouple location index, [–]	liq	–	liquidus, [–]
b	–	bottom surface, [–]	max	–	maximum, [–]
eff	–	effective value, [–]	r	–	rear (Goldak), [–]
exp	–	experimental, [–]	sim	–	simulated, [–]
f	–	front (Goldak), [–]	t	–	top surface, [–]

Superscripts

exp	–	experimental, [–]	sim	–	simulated, [–]

Abbreviations and acronyms

FDM	–	finite difference method, [–]	GRG	–	grey relational grade, [–]
GMAW	–	gas metal arc welding, [–]	LHS	–	latin hypercube sampling, [–]
GRA	–	grey relational analysis, [–]	SOR	–	successive over-relaxation, [–]
GRC	–	grey relational coefficient, [–]	TC	–	thermocouple, [–]

References

[1] ***, Standard - Numerical welding simulation - Execution and documentation, ISO 18166:2026, International Organization for Standardization, ISO, https://www.iso.org/standard/88390.html

[2] Nascimento, E. J. G., et al., A literature review in heat source thermal modeling applied to welding and similar processes, *Int. J. Adv. Manuf. Technol.*, *126* (2023), 7, pp. 2917–2957, DOI: 10.1007/s00170-023-11253-z

[3] Goldak, J., et al., A new finite element model for welding heat sources, *Metall. Trans. B*, *15* (1984), 2, pp. 299–305, DOI: 10.1007/BF02667333

[4] Kik, T., Calibration of heat source models in numerical simulations of welding processes, *Metals*, *14* (2024), 11, 1213, DOI: 10.3390/met14111213

[5] DuPont, J. N., Thermal efficiency of arc welding processes, *Weld. J.*, *74* (1995), 12, pp. 406s–416s

[6] Haelsig, A., et al., New findings on the efficiency of gas shielded arc welding, *Weld. World*, *56* (2012), 11–12, pp. 98–104, DOI: 10.1007/BF03321400

[7] De Deus, V. S., et al., Prediction of the Emissivity Curve at High Temperatures of Low Carbon Steel, *J. Mater. Sci. Res.*, 9 (2020), 2, pp. 59–70, DOI:10.5539/jmsr.v9n2p59.

[8] Goyal, R., et al., A Model Equation for the Convection Coefficient for Thermal Analysis of Welded Structures, Proceedings, (Eds. S. David et al.), 8th International Conference on Trends in Welding Research, Pine Mountain, GA, USA, 2008, pp. 321–327, DOI:10.1361/cp2008twr321

[9] Sun, J., et al., Effects of heat source geometric parameters and arc efficiency on welding temperature field, residual stress, and distortion in thin-plate full-penetration welds, *Int. J. Adv. Manuf. Technol.*, *99* (2018), 1, pp. 497–515, DOI: 10.1007/s00170-018-2516-6

[10] Azar, A. S., et al., Determination of welding heat source parameters from actual bead shape, *Comput. Mater. Sci.*, *54* (2012), pp. 176–182, DOI: 10.1016/j.commatsci.2011.10.025

[11] Walker, T. R., Bennett, C. J., An automated inverse method to calibrate thermal finite element models for numerical welding applications, *J. Manuf. Process.*, *47* (2019), pp. 263–283, DOI: 10.1016/j.jmapro.2019.09.021

[12] Rissaki, D., et al., Establishing an automated heat-source calibration framework, in: *Mathematical Modelling of Weld Phenomena* (Eds. C. Sommitsch, et al.), Graz University of Technology, Graz, Austria, 2023, pp. 221–236, DOI: 10.3217/978-3-85125-968-1-12

[13] Bjelić, M. B., et al., Numerical modeling of two-dimensional heat-transfer and temperature-based calibration using simulated annealing optimization method: Application to gas metal arc welding, *Therm. Sci.*, *20* (2016), 2, pp. 655–665, DOI: 10.2298/TSCI150415127B

[14] Bjelić, M. B., et al., Multi-objective calibration of the double-ellipsoid heat source model for GMAW process simulation, *Therm. Sci.*, *26* (2022), 3A, pp. 2081–2092, DOI: 10.2298/TSCI210131181B

[15] Viana, F. A. C., A tutorial on Latin Hypercube design of experiments, *Qual. Reliab. Eng. Int.*, *32* (2016), 5, pp. 1975–1985, DOI: 10.1002/qre.1924

[16] Deng, J. L., Introduction to grey system theory, *J. Grey Syst.*, *1* (1989), 1, pp. 1–24

[17] Fujiyama, S., et al., Dependency of arc efficiency on welding current in gas metal arc welding, *Q. J. Jpn. Weld. Soc.*, *40* (2022), 4, pp. 9WL–12WL, DOI: 10.2207/qjjws.40.9WL

[18] Kolařík, L., et al., Verification of the efficiency coefficient of the welding process by the CMT welding method, *Int. J. Adv. Manuf. Technol.*, *135* (2024), 11–12, pp. 5911–5924, DOI: 10.1007/s00170-024-14854-4

Submitted: 20.03.2026.
Revised: 15.03.2026.
Accepted: 02.04.2026.